PAPER

High-performance deep-learning based polarization computational ghost imaging with random patterns and orthonormalization

Physica Scripta

PAPER

High-performance deep-learning based polarization computational ghost imaging with random patterns and orthonormalization

Chenxiang Xu[1], **Dekui Li**[1], **Xueqiang Fan**[1], **Bing Lin**[1], **Kai Guo**[1], **Zhiping Yin**[2] **and Zhongyi Guo**[1,*]

[1] School of Computer and Information, Hefei University of Technology, Hefei, 230009, People's Republic of China
[2] School of Instrument Science and Opto-electronics Engineering, Hefei University of Technology, Hefei, 230009, People's Republic of China
[*] Author to whom any correspondence should be addressed.

E-mail: guozhongyi@hfut.edu.cn

RECEIVED
17 January 2023

REVISED
28 March 2023

ACCEPTED FOR PUBLICATION
26 April 2023

PUBLISHED
9 May 2023

Keywords: polarization computational ghost imaging (PCGI), Improved U-net (IU), orthonormalization

Abstract

Polarization computational ghost imaging (PCGI) often requires a large number of samples to reconstruct the targets, which can be optimized by reducing sampling rates with the aids of deep-learning technology. In this paper, the random patterns and successive orthonormalization instead of common Hadamard patterns, has been introduced into the deep-learning based PCGI system to recover high-quality images at lower sampling rates. Firstly, we use a polarized light to illuminate the target with random patterns for sampling. Then we can obtain a vector of bucket detector values containing the reflective information of the target. Secondly, we orthonormalize the vector according to the random patterns. Subsequently, the orthonormalized data can be input into the Improved U-net (IU-net) for reconstructing the targets. We demonstrate that higher-quality image of the testing sample can be obtained at a lower sampling rate of 1.5%, and superior-generalization ability for the untrained complex targets can be also achieved at a lower sampling rate of 6%. Meanwhile, we have also investigated the generalization ability of the system for the untrained targets with different materials that have different depolarization properties, and the system still demonstrates superior performances. The proposed method may pave a way towards the real applications of the PCGI.

1. Introduction

Computational ghost imaging (CGI) has developed rapidly with the developments of modulating ability for the optical fields in recent years [1, 2]. Meanwhile, the CCD camera on the reference arm can be omitted, imaging with a single-arm light path and a barrel detector [3, 4]. It simplifies the light path and improves the performance of ghost imaging. In comparison to traditional imaging, CGI has already prohibited great potentials in applications, such as single-pixel imaging [5, 6], biological imaging [7–10], information encryption [11–13], laser radar technique [14, 15] and imaging through atmospheric turbulence environment [16–21]. However, the reflectivity or transmittance of targets are sometimes close to the background in many real-world scenarios, making it difficult to identify the targets from the background by the received light intensity. Fortunately, there always exists difference in polarization characteristics between the targets and the backgrounds. Moreover, polarized lights also have good anti-scattering effects [22–25]. Therefore, polarization computational ghost imaging provides additional information for contrast-enhanced target recognition in traditional ghost imaging [26–29].

However, the CGI often requires a large number of samples and high-cost. In recent years, deep-learning based CGI [30–33] has rapidly developed in the image classification [34] and image tracking [35], since it can greatly reduce the sampling time and improve the CGI efficiency. In these processes, the original images and low-quality images recovered from the CGI are used as labels and input of the network, respectively, and high-quality images can be obtained through the iterative training network [36, 37]. Compared to previous algorithms, deep-learning based methods demonstrate faster and more robust reconstructions. Nowadays, most

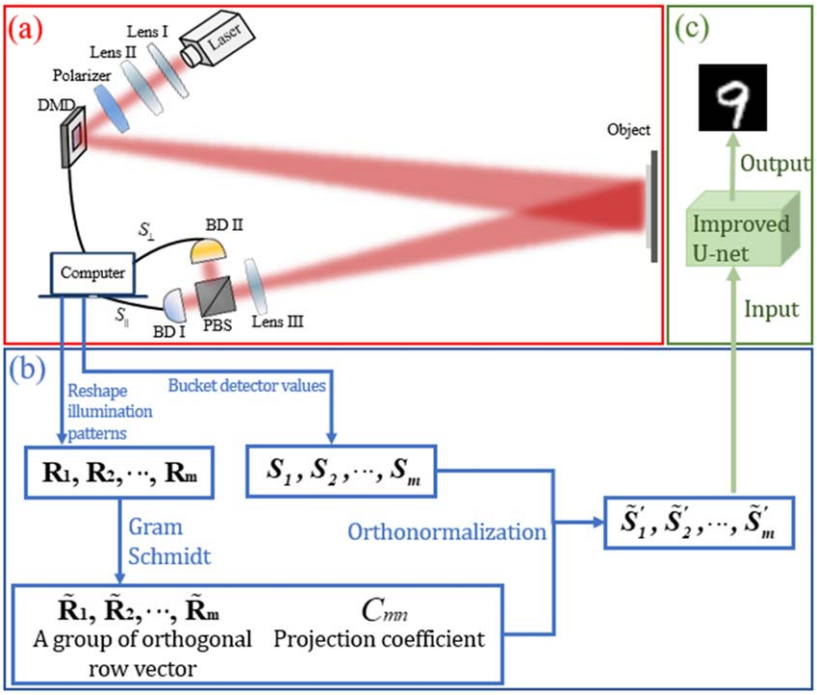

Figure 1. The flow chart of our scheme: (a) Schematic diagram of the optical setup; (b) Data processing with orthonormalization; (c) The IU-net recover target.

researchers use structured light with Hadamard patterns to sample the target in deep-learning based CGI [38]. With the orthogonal characteristics, Hadamard patterns can reduce the influence of scattering medium on the CGI's signal-to-noise ratio and obtain a clearer image [39, 40]. However, the Hadamard patterns have special mathematical properties that affect the sampling efficiency. Hadamard patterns often appear in chunks, and this characteristic lead to significant difference in sampling efficiency between different targets. Especially at low sampling rates, it is difficult to train the network by using the input obtained from CGI with Hadamard patterns.

In this paper, we introduce a random illuminated pattern into the Improved U-net (IU-net) based PCGI scheme, and the inputs of IU-net are the values obtained by bucket detector after orthonormalization [12, 41, 42], which can be called as the random-pattern orthonormalization for the IU-net based PCGI (RPO-IU-PCGI). It is worth noting that the random pattern indicates irregular distribution of the pattern, which is generated by a digital micromirror device (DMD) instead of a thermal or pseudo-thermal light. The obtained data is preprocessed by orthonormalization which will not change the relation between the reference patterns and bucket detector values. The orthonormalized values are used as the input of the IU-net. Our solution can accurately recover the target image at a very low sampling rate, and has good generalization in complex targets and different depolarization properties. For validation, the imaging results obtained from deep-learning based PCGI with the proposed method and Hadamard patterns are compared. We hope the proposed method could provide a new chance for the application of the PCGI.

2. Methodology

The optical setup for the proposed scheme is shown in figure 1(a). The light launched from a laser undergoes through two lens and a polarizer, and random patterns are generated through DMD after the polarized light passing. DMD is controlled by a computer. A polarization beam splitter (PBS) divides the polarized light reflected from the target into horizontally and vertically polarized lights, which are collected by bucket detectors (BD) I and II, respectively. Thereupon, the intensities of horizontally and vertically components are obtained as $S_{\parallel}$ and $S_{\perp}$, respectively. For conventional CGI, the target can be reconstructed by [27]:

$$O(x, y) = \langle R(x, y)S\rangle_m - \langle R(x, y)\rangle_m \langle S\rangle_m, \tag{1}$$

where $R(x,y)$ is the pattern after the DMD, S is the intensity value obtained at bucket detector, i.e. $S_t = S_{\parallel} + S_{\perp}$, $\langle\cdot\rangle_m$ indicates the statistical average operator and m represents the number of measurement time. For the PCGI, the value of $S_p = S_{\parallel} - S_{\perp}$ is used as the intensity S in equation (1). The difference between $S_{\parallel}$ and $S_{\perp}$ contains the polarization information of the target [27], which will benefit to improve the imaging quality. For unknown

targets, we do not know its depolarization characteristics. The target information (horizontal and vertical polarization light) can still be obtained by two bucket detectors combined with a polarization beam splitter, which is consistent with traditional polarization imaging principle.

2.1. Orthonormalization

Supposing that the object is 'O' and the illuminating patterns are '$\mathbf{R}_1$, $\mathbf{R}_2$ $\cdots$,$\mathbf{R_m}$', the whole CGI in mathematics can be expressed as:

$$\left(R=\begin{bmatrix} R_1(1,1) & R_1(2,1) & \cdots & R_1(x,y) \\ R_2(1,1) & R_2(2,1) & \cdots & R_2(x,y) \\ \vdots & \vdots & \vdots & \vdots \\ R_x(1,1) & R_x(2,1) & \ddots & R_x(x,y) \\ \vdots & \vdots & \vdots & \vdots \\ R_{\mathrm{m}}(1,1) & R_m(2,1) & \cdots & R_m(x,y) \end{bmatrix}\right)\cdot\left(O=\begin{bmatrix} O(1,1) \\ O(2,1) \\ \vdots \\ O(x,1) \\ \vdots \\ O(x,y) \end{bmatrix}\right)=\left(S=\begin{bmatrix} S_1 \\ S_2 \\ \vdots \\ S_x \\ \vdots \\ S_m \end{bmatrix}\right) \tag{2}$$

From equation (2), it can be seen that it is more like solving an equation to recover image (O) by the CGI. If all the patterns have orthogonality, it is helpful to solve this equation. However, the random patterns don't have orthogonal characteristics, so we have to optimize the data by using orthonormalization if we want to use the random patterns.

Figure 1(b) show the data processing with orthonormalization. In our scheme, the Gram-Schmidt and normalization processes are performed on the value of bucket detector [12]. To this end, a group of projection coefficient should be calculated from the value of illumination patterns, and can be expressed as:

$$Cmn=\frac{\widetilde{\mathbf{R}}_{\mathbf{n}}\cdot\mathbf{R_m}}{\widetilde{\mathbf{R}}_{\mathbf{n}}\cdot\widetilde{\mathbf{R}}_{\mathbf{n}}}, \tag{3}$$

$$\begin{aligned} &\widetilde{\mathbf{R}}_1=\mathbf{R}_1, \\ &\widetilde{\mathbf{R}}_2=\mathbf{R}_2-C_{21}\cdot\widetilde{\mathbf{R}}_1, \\ &\widetilde{\mathbf{R}}_3=\mathbf{R}_3-C_{31}\cdot\widetilde{\mathbf{R}}_1-C_{32}\cdot\widetilde{\mathbf{R}}_2, \\ &\cdots \\ &\widetilde{\mathbf{R}}_{\mathbf{m}}=\mathbf{R_m}-\sum_{n=1}^{m-1}C_{mn}\cdot\widetilde{\mathbf{R}}_{\mathbf{n}}, \end{aligned} \tag{4}$$

where Cmn is the projection coefficient, $\mathbf{R}_1$, $\mathbf{R}_2$, $\cdots$,$\mathbf{R_m}$ are the row vector obtained from the reshaped illumination patterns, 'reshaped' is to convert a matrix of size 64*64 into a vector of 4096*1, where the value will not change. $\tilde{\mathbf{R}}_1$, $\tilde{\mathbf{R}}_2$, $\cdots$,$\tilde{\mathbf{R}}_{\mathbf{m}}$ mean a group of orthogonal row vector calculated from $\mathbf{R}_1$, $\mathbf{R}_2$, $\cdots$,$\mathbf{R_m}$ by equation (4). Each bucket detector value can be acquired by illuminating the target with one pattern, so the illuminating patterns and the bucket detector value belong to a one-to-one correspondence. We will post-process the patterns, so we need to perform same mathematical operation for the bucket detector values. By orthonormalizing process, the new values of bucket detectors $\tilde{S}_1'$, $\tilde{S}_2'$, $\cdots$,$\tilde{S}_m'$ can be created and written as:

$$\begin{aligned} &\tilde{S}_1=S_1, \\ &\tilde{S}_2=S_2-C_{21}\cdot\tilde{S}_1, \\ &\tilde{S}_3=S_3-C_{31}\cdot\tilde{S}_1-C_{32}\cdot\tilde{S}_2, \\ &\cdots \\ &\tilde{S}_m=S_m-\sum_{n=1}^{m-1}C_{mn}\cdot\tilde{S}_n, \end{aligned} \tag{5}$$

$$\tilde{S}_m'=\tilde{S}_m/\|\tilde{R}_m\|, \tag{6}$$

where S_1, S_2, $\cdots$,S_m are the original values from BD. One may refer to [12] for details of the orthonormalization process. After the above orthonormalization process, the relation between the reference patterns and the bucket detector values is well maintained. Therefore, the orthonormalized bucket detector values can be used as the input to the deep-learning network as show in figure 1(c), and meanwhile, the original images are used as the labels.

2.2. Architecture of Improved U-net

Since bucket detector values contain information of the target, the network can learn the target features and recover the image. Herein, we use an IU-net [43] based deep-learning network, as shown in figure 2. The DenseNet [44, 45] network is used as the feature extraction layer of the IU-net. In the training process, due to increasing number of network layers, the backpropagation process is easy to lead to gradient vanishing and gradient explosion. In our network, the shallow and deep features are connected by introducing the skip connection, from which the gradient update can consider the multi-layer weight information together when

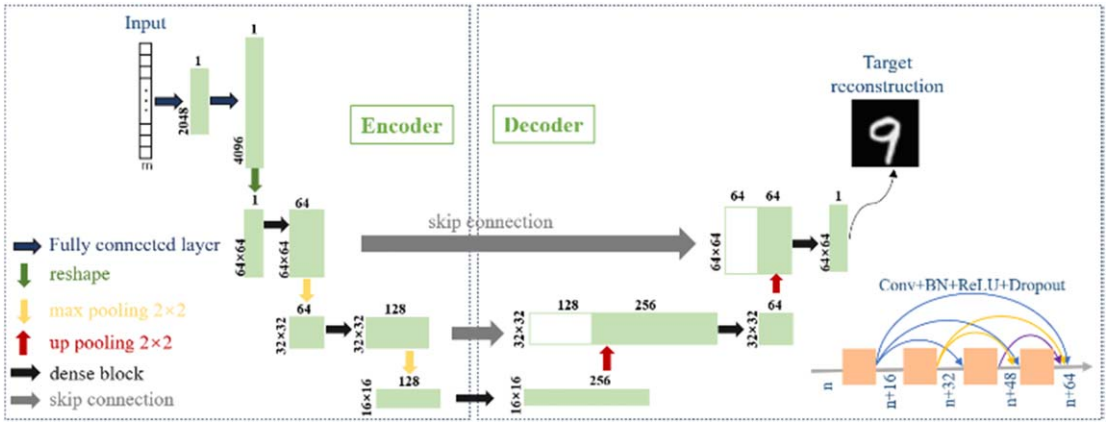

Figure 2. Schematic diagram of IU-net structure.

Table 1. Mueller matrix elements.

Material	m_{22}	m_{44}
Steel	0.975	0.99
Stone	0.385	0.35
Wood	0.215	0.16

performing long-distance feature extraction. Each encoder consists of three layers: dense block layer, dropout layer and max pooling layer. The difference between the encoder and decoder is that the last layer of each decoder uses the up-pooling layer. In fact, the DenseNet is a composite layer composed of four dense blocks, and each of them is connected to next all blocks. It makes the transfer of features and gradients more effective, and the training process for the IU-net will also be easier.

The workflow of the utilized deep-learning network is described in the following. The first layer is an input layer which inputs a one-dimensional vector after orthonormalization process. The second and third layers are fully connected layers with sizes of 2048 × 1 and 4096 × 1, respectively. The fourth layer, a vector-to-matrix layer, reshapes the vector with size of 4096 × 1 to a matrix with size of 64 × 64. The temporary image [33] enters a network of U-net structures, thereby the statistical relation between matrix and the original target can be obtained based on the IU-net encoder-decoder architecture. The convolutional layer in DenseNet uses a filter with the kernel size of 3 × 3. As the numbers of both network and filter layers increase, a max pooling layer with a step size of 2 × 2 reduces the dimension of the high-resolution image to half of the original. In addition, the decoder is equivalent to the inverse process of encoder. Each decoder is also three layers, the last layer of each decoder uses the up-pooling layer, which is an opposite process of max pooling and increases the dimension of the low-resolution input image. After the above encoder and decoder processes, we may get an image with size of 64 × 64. In the whole network model, the activation function is a rectified linear unit (ReLU), making the IU-net training quicker and more efficient. At the same time, the dropout layer is adopted to reduce overfitting. The IU-net network guarantees the validity of the results, and reduces computational complexity.

3. Result and discussion

In order to investigate, an object with two parts is imaged in our proposed system, as shown in the inset of figure 1. The digit in the middle part of the object is made of steel with high reflectivity and low depolarization characteristic. The rest parts are the background made of stone with high reflectivity, high depolarization properties. For comparison, we choose materials of steel, stone and wood as the targets and backgrounds here, and their Mueller matrix parameters, describing depolarization characteristics, are summarized in table 1 [46].

We define the sampling rate as $\alpha = m/N$, where m and N are the sampling number and the size of the full image respectively. Figure 3 shows the superiority of PCGI with orthonormalization over the conventional CGI. It presents imaging results with random patterns and full sampling rate ($\alpha = 100\%$), from figures 3(a) to (d) corresponding to the PCGI with orthonormalization, CGI with orthonormalization, PCGI without

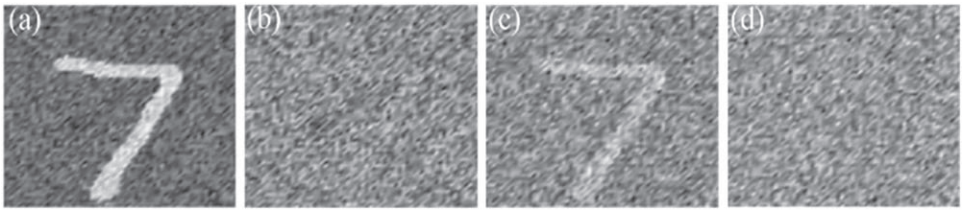

Figure 3. Imaging with different conditions: (a) $S = S_p$, imaging by the PCGI with orthonormalization process; (b) $S = S_t$, imaging by the CGI with orthonormalization process; (c) $S = S_p$, imaging by the PCGI without orthonormalization process; (d) $S = S_t$, imaging by the CGI without orthonormalization process.

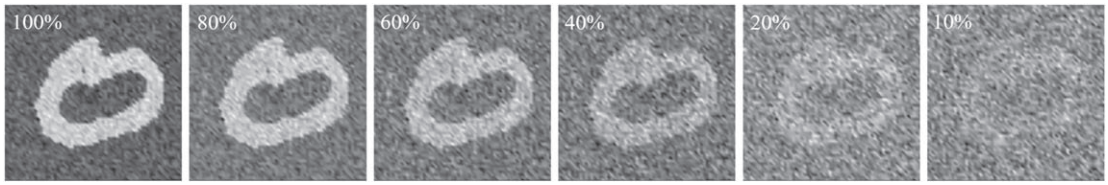

Figure 4. Imaging by the PCGI with orthonormalization at different sampling rates.

orthonormalization, and CGI without orthonormalization. The size of the results in figure 3 is 64*64. It can be seen that the introduction of polarization and orthonormalization into the CGI may significantly improve the imaging performance with the random patterns.

We also tested the recovery effect with orthonormalization at different α. It presents imaging results by the PCGI with orthonormalization as shown in figure 4. As the α decreases, the image quality gradually decreases. When the α reaches 20%, the image has become blurry and completely invisible in the sampling rate of 10%. So we will use deep-learning techniques for clearly recovering targets at lower α.

3.1. Model implementation

Indeed, higher sampling rate could help us obtain high-quality images. However, it may cost much more time, so, it is highly desired to restore better images with lower costs. Herein, the IU-net is used to restore high-quality targets at very low sampling rates. To test the proposal, the MNIST dataset [47] of grayscale images of handwritten digits (0–9) is considered as a standard set of objects, consisting of 5000 images with size of 64×64. Our simulation environment is an ideal state, which is regardless of environmental interference and instrument performance. In simulations, the objects are divided into two parts. The digit and background are made of steel and stone, respectively. During the PCGI with random patterns, the sampling rates are very low, ranging from 1% to 25%. A set of bucket detector values are obtained and input into the IU-net after orthonormalization. Due to the difference in sampling rates, the target information obtained at different sampling rates is inconsistent. So, we have to train network separately at different sampling rates. The percentages of the training, verification, and testing sets are 90%, 5%, and 5%, respectively. The optimizer is stochastic gradient descent (SGD) with added momentum, and the learning rate is 0.01. Twenty epochs are used for the training process. Negative Pearson Correlation Coefficient (NPCC) [48, 49] are widely used in the loss function of various neural networks and can be expressed as:

$$NPCC = \frac{-\sum_{i=1}^{w}\sum_{j=1}^{h}(Y(i,j)-Y_1)(G(i,j)-G_1)}{\sqrt{\sum_{i=1}^{w}\sum_{j=1}^{h}(Y(i,j)-Y_1)^2}\sqrt{\sum_{i=1}^{w}\sum_{j=1}^{h}(G(i,j)-G_1)^2}}, \tag{7}$$

where G_1 and Y_1 are the mean values of the ground truth G and the network output Y, respectively. The training of the model is carried out in an image processing unit (NVIDIA RTX 3090), using the pytorch framework with Python 3.6. In our experiments, the concrete training time was 37.4379 min (2246.27 s), and the verification time is 0.026 s.

3.2. Comparison of results

The object can be clearly recovered from our IU-net even though the sampling rate of the PCGI is very low, for both cases with Hadamard patterns and orthonormalization random patterns. In order to demonstrate, we plot

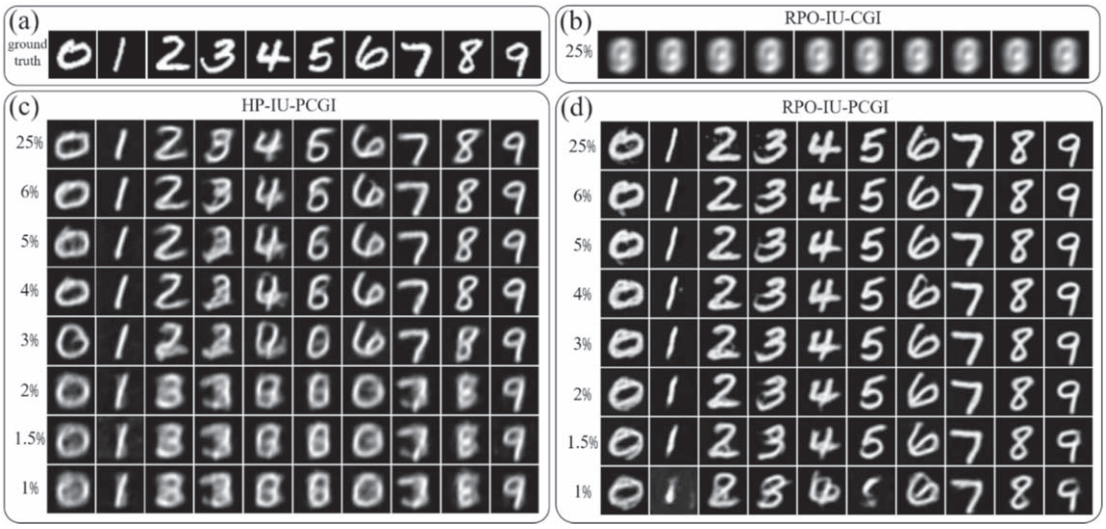

Figure 5. Imaging effects at different sampling rates: (a) ground truth; (b) RPO-IU-CGI reconstructing objects; (c) HP-IU-PCGI reconstructing objects; (d) RPO-IU-PCGI reconstructing objects.

the images obtained from the proposed deep-learning framework. In these cases, the sampling rates are too low to restore the object directly from both CGI and PCGI methods. The size of the results in figure 5 is 64*64. Figure 5(a) shows the images of the ground truth for comparison. Figure 5(b) is the resulted images from the random-pattern orthonormalization for the IU-net based CGI (RPO-IU-CGI), in which the input is $S = S_t$, and the sampling rate is $\alpha = 25\%$. Obviously, it could be difficult to recover the object when the sampling rate is lower for the RPO-IU-CGI, even with the help of our IU-net. In contrast, the object can be completely recovered from the RPO-IU-PCGI with low sampling rates of $\alpha = 25\%$ (m = 1024), 6% (m = 246), 5% (m = 205), 4% (m = 164), 3% (m = 123), 2% (m = 82), 1.5% (m = 62), and 1% (m = 41) respectively, as shown in figure 5(d). Even for $\alpha = 1.5\%$, an extremely low sampling rate, the digits can be still well recognized from the background. For the Hadamard-patterns IU-net based PCGI (HP-IU-PCGI) with the sampling rate of $\alpha = 25\%$, 6%, 5%, 4%, 3%, 2%, 1.5%, and 1%, blurred images are observed, as shown in figure 5(c), which should be attributed to the intensive speckles on Hadamard patterns. When $\alpha = 6\%$, the digits of '3' and '5' are almost undistinguishable from the background. When the value of α decreases, more images become blurred and vague, leading to the nullity of the IU-net.

To quantitatively evaluate the performance of the proposed framework, we calculated the peak signal-to-noise ratio (PSNR) and structural similarity index (SSIM) of the results in the ranging from 1% to 6%. The PSNR can be defined as:

$$\mathrm{PSNR} = 10 \times \log_{10}\frac{255^2}{\mathrm{MSE}}, \tag{8}$$

where MSE indicates the mean square error. SSIM is usually used to measure the similarity of images, consisting of brightness, contrast, and structure. Supposing two images X and Y, the SSIM can be calculated by:

$$SSIM(X,\ Y) = \frac{(2\mu_X\mu_Y + C_1)(2\sigma_{XY} + C_2)}{(\mu_X^2 + \mu_Y^2 + C_1)(\sigma_X^2 + \sigma_Y^2 + C_2)}, \tag{9}$$

where μ_X and μ_Y are the averages of X and Y respectively, σ_X and σ_Y are the variances of X and Y respectively, σ_{XY} is the covariance of X and Y, C_1 and C_2 are two minor positive constants used to avoid a null denominator. The value of SSIM ranges from 0 to 1. The larger the SSIM value, the higher the image similarity, and SSIM = 1 indicates that X and Y are exactly the same.

The dependences of calculated PSNR and SSIM (from 250 results of testing sets) on the sampling rate are plotted in figure 6. It can be seen that when sampling rate α is lower, the values of PSNR and SSIM are smaller for both HP-IU-PCGI and RPO-IU-PCGI. However, the values of PSNR and SSIM of RPO-IU-PCGI are much larger than those of HP-IU-PCGI when the values of α are the same. More importantly, the PSNR of HP-IU-PCGI with $\alpha = 6\%$ is comparable with that of RPO-IU-PCGI with $\alpha = 1\%$, while the SSIM of HP-IU-PCGI with $\alpha = 6\%$ is close to that of RPO-IU-PCGI with $\alpha = 2\%$. These results are consistent with the results in figures 5(c) and (d), further demonstrating the superiority of our proposed RPO-IU-PCGI.

The superior performance of the RPO-IU-PCGI over the HP-IU-PCGI might be attributed to the following reasons. First, the size of the minimum lump of gray value in ghost images is proportional to the speckle size of

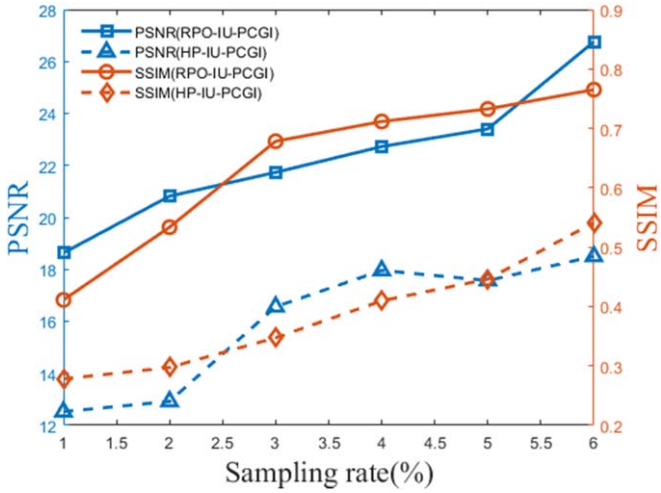

Figure 6. PSNR and SSIM of the results in the ranging by RPO-IU-PCGI and HP-IU-PCGI with the α from 1% to 6%.

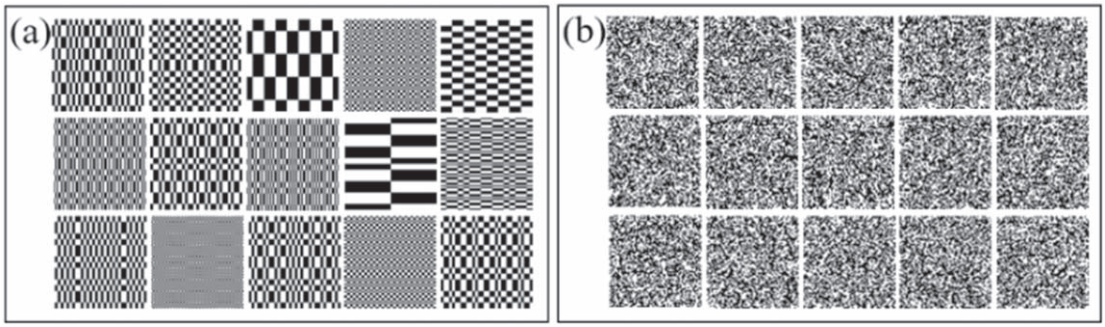

Figure 7. (a) Hadamard patterns; (b) Random patterns.

sampling pattern. As a result, massive loss of the image details will happen when the speckle size is large. Figure 7(a) shows a set of Hadamard patterns which are randomly selected. From space structure of the Hadamard patterns, it is prone to appear concentrated together in bright or dark pixels, which will lead to so many concentrated areas of the target information without collecting for the experiment at lower sampling rate ($<$25%). It is easy to see that most of them exhibit speckle patterns with large size, leading to degradation of images quality. Second, the sampling effect of different Hadamard patterns are significantly different with each other especially when speckle size is large. It results in large distinction in target features obtained by the bucket detector each time. Therefore, it is difficult for the IU-net to extract the target's features with the bucket detector values obtained by the Hadamard patterns at a very low sampling rate. In contrast, the random sampling patterns do not face with such challenges since their speckle size is much smaller and uniformly and randomly distributed, as shown in figure 7(b).

3.3. Generalization

We further explore the generalization of our proposed RPO-IU-PCGI. We design the targets of Chinese characters and English letters. The targets and background are made of steel and stone, respectively. Although the IU-net has been trained by using the MNIST handwritten dataset, it is clearly seen that it can be used to reconstruct the images of Chinese characters and English letters without training, as shown in figure 8(a). The PSNR and SSIM based on these results in figure 8(a) at different sampling rates, have also been demonstrated in figure 8(b). The target can be recovered very well when the α is 6%, demonstrating that our scheme can be generalized at a very low sampling rate. As the sampling rate decreases, it becomes difficult to recover these complex targets, especially the Chinese characters. For English letters that have not been trained, at a sampling rate of 5%, one may still discriminate the targets.

We further explore the generalization of our proposed RPO-IU-PCGI for the targets with different materials. As mentioned earlier, the objects of the dataset for the IU-net training are composed of steel and

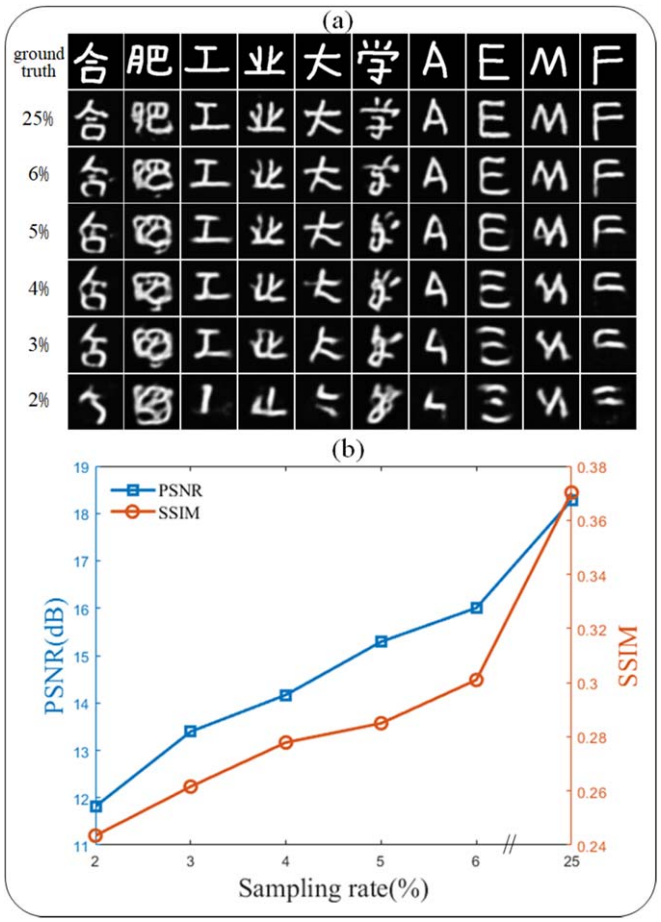

Figure 8. (a) Network generalization test results at different α; (b) The PSNR and SSIM of generalization test results at different α.

stone. To verify the generalization of the network, we make the digit and background are made of steel and wood, respectively, which have not been trained. The depolarization properties of wood is very high, and very different with that of steel [46]. The top panel of figure 9 shows the images of the ground truth for comparison. The results of RPO-IU-PCGI at different α are shown in figure 9(a), where the targets can be recovered very accurately. Even the targets are made of untrained materials, we can still take advantage of differences in their depolarization properties to recover them using our network. As long as the depolarization properties of the target and the background are obviously different, our scheme can accurately restore the target at a very low sampling rate.

In a practical situation, we cannot rule out the fact that the depolarization properties of the target and the surrounding background may be very similar. So we have also explored the generalization of IU-net when the depolarization properties of both the target and the background are similar. Figure 9(b) shows the results that the digit and background are made of stone and wood, respectively. Due to the similarity of the depolarization properties [46], the target is un-distinguishable when the sampling rate is extremely low. Fortunately, it can be seen that the recovery target can be clear at a sampling rate of 25%.

4. Conclusion

In this paper, we have introduced random patterns into deep-learning based polarization computational ghost imaging system to recover high-quality images at a low sample rate. The object was illuminated with the random patterns. A modified deep learning network is used to automatically learn the mapping relationship between the target and bucket detector values. The obtained data was orthonormalized and inputted into the IU-net. Compared with the results obtained with Hadamard patterns, we demonstrated higher-quality images at a low sample rate of 1.5% and superior generalization at a low sample rate of 6%. This is due to the superiority of the random patterns over the Hadamard patterns for the intensive speckles. We have also demonstrated the generalization of the designed RPO-IU-PCGI. For complex targets or materials that have not been trained, the targets can be also accurately recovered at extremely low sampling rates. The proposed method may promote the

Figure 9. Generalization effects of the RPO-IU-PCGI for the targets with in different materials: (a) The results for the target and background consisting of steel and wood at different α; (b) The results for the target and background consisting of stone and wood at different α.

practical applications of polarization computational ghost imaging, such as target identification, biomedical, military and so on.

Data availability statement

The data cannot be made publicly available upon publication because they are not available in a format that is sufficiently accessible or reusable by other researchers. The data that support the findings of this study are available upon reasonable request from the authors.

Funding

National Natural Science Foundation of China (61775050).

Disclosures

The authors declare no conflicts of interest.

ORCID iDs

Kai Guo https://orcid.org/0000-0002-0676-7371
Zhongyi Guo https://orcid.org/0000-0001-7282-2503

References

[1] Shapiro J H 2008 Computational ghost imaging *Phys. Rev.* **78** 061802
[2] Gao R K, Yan L S, Xu C X, Li D K and Guo Z Y 2021 Two key technologies influencing on computational ghost imaging quality *Laser Optoelectron.* **58** 1811011
[3] Chen J, Gong W L and Han S S 2013 Sub-Rayleigh ghost imaging via sparsity constraints based on a digital micro-mirror device *Phys. Lett.* **377** 1844–7
[4] Gong W L and Han S S 2011 Correlated imaging in scattering media *Opt. Lett.* **36** 394–6
[5] Feng J, Jiao S, Gao Y, Lei T and Du L 2020 Design of optimal illumination patterns in single-pixel imaging using image dictionaries *IEEE Photonics J.* **12** 1–9 Art no. 6901509
[6] Shen S, Gu G, Mao T, Chen Q, He W and Shi J 2022 Pseudo-Random spread spectrum technique based single-pixel imaging method *IEEE Photonics J.* **14** 1–9 Art no. 5631409

[7] He Y H, Zhang A X, Huang Y Y, Yu W K, Chen L M and Wu L A 2020 Spectroscopic x-ray ghost imaging *2020 Conf. on Lasers and Electro-Optics Pacific Rim (CLEO-PR)* 1–2
[8] Yu H, Lu R, Tan Z, Zhu R and Han S 2017 X-ray fourier-transform ghost imaging via sparsity constraints *2017 IEEE Nuclear Science Symp. and Medical Imaging Conf. (NSS/MIC)*. 1–3
[9] Schori A, Borodin D, Tamasaku K and Shwartz S 2018 Ghost Imaging with paired x-ray photons *2018 Conf. on Lasers and Electro-Optics (CLEO)*. 1–2
[10] Zhang A X, He Y H, Wu L A, Chen L M and Wang B B 2018 Tabletop x-ray ghost imaging with ultra-low radiation *Optica.* **5** 374–7
[11] Kong L J, Li Y N, Qian S X, Li S M, Tu C H and Wang H T 2013 Encryption of ghost imaging *Phys. Rev.*A **88** 13852
[12] Wu J, Chen Y, Zhou C, Chen Z, Xu C and Song L 2022 A remote security computational ghost imaging method based on quantum key distribution technology *IEEE Access.* **10** 18899–909
[13] Clemente P, Durán V, Torres-Company V, Tajahuerce E and Lancis J 2010 Optical encryption based on computational ghost imaging *Opt. Lett.* **35** 2391–3
[14] Wang Z *et al* 2022 Ghost imaging of moving target based on the periodic pseudo-thermal light field generated by a 2D silicon OPA *IEEE Photonics J.* **14** 1–8 Art no. 6613408
[15] Ma S, Liu Z T, Wang C L, Hu C Y, Li E R, Gong W L, Tong Z S, Wu J R, Shen X and Han S S 2019 Ghost imaging LiDAR via sparsity constraints using push-broom scanning *Opt. Express* **27** 13219–28
[16] Zhang P L, Gong W L, Shen X and Han S S 2010 Correlated imaging through atmospheric turbulence *Phys. Rev.*A **82** 033817
[17] Cheng J 2009 Ghost imaging through turbulent atmosphere *Opt. Express* **17** 7916–21
[18] Wang X, Xi J and Yang F 2020 An effective computational ghost imaging based on noise estimation and elimination *IEEE Access.* **8** 175513–20
[19] Gao Z *et al* 2020 Computational ghost imaging in scattering media using simulation-based deep learning *IEEE Photonics J.* **12** 1–15 Art no. 6803115
[20] Li D, Yang D, Sun S, Li Y G, Jiang L, Lin H Z and Liu W T 2021 Enhancing robustness of ghost imaging against environment noise via cross-correlation in time domain *Opt. Express* **29** 31068–77
[21] Tan W, Huang X W, Nan S Q, Bai Y F and Fu X Q 2020 Ghost imaging through inhomogeneous turbulent atmosphere along an uplink path and a downlink path *OSA Continuum.* **3** 1222–31
[22] Li D K, Xu C X, Zhang M, Wang X Y, Guo K, Sun Y X, Gao J and Guo Z Y 2021 Measuring glucose concentration in a solution based on the indices of polarimetric purity *Biomed. Opt. Express* **12** 2447–59
[23] Li D K, Guo K, Sun Y X, Bi X, Gao J and Guo Z Y 2021 Depolarization characteristics of different reflective interfaces indicated by indices of polarimetric purity (IPPs) *Sensors* **21** 1221
[24] Shen F, Zhang M, Guo K, Zhou H P, Peng Z Y, Cui Y M, Wang F, Gao J and Guo Z Y 2019 The depolarization performances of scattering systems based on the Indices of polarimetric purity (IPPs) *Opt. Express* **27** 28337–49
[25] Wang X Y, Hu T W, Li D K, Guo K, Gao J and Guo Z Y 2020 Performances of polarization-retrieve imaging in stratified dispersion media *Remote Sens.* **12** 2895
[26] Shi D F, Hu S X and Wang Y J 2014 Polarimetric ghost imaging *Opt. Lett.* **39** 1231–4
[27] Zhu Y C, Shi J H, Yang Y and Zeng G H 2015 Polarization difference ghost imaging *Appl. Opt.* **54** 1279–84
[28] Zhu Y C, Shi J H, Li H and Zeng G H 2014 Visibility and contrast enhancement with polarization difference ghost imaging *2014 Conf. on Lasers and Electro-Optics (CLEO) - Laser Science to Photonic Applications* 1–2
[29] Li D K, Xu C X, Yan L S and Guo Z Y 2022 High-performance scanning-mode polarization based computational ghost imaging (SPCGI) *Opt. Express* **30** 17909–21
[30] Zhu Y L, She R B, Liu W Q, Lu Y F and Li G Y 2022 Deep learning optimized terahertz single-pixel imaging *IEEE Trans. Terahertz Sci. Technol.* **12** 165–72
[31] Garcia J M, Prophet R, Michel J C F, Ebelt R, Vossiek M and Weber I 2019 Identification of ghost moving detections in automotive scenarios with deep learning *2019 IEEE MTT-S Int. Conf. on Microwaves for Intelligent Mobility (ICMIM)* 1–4
[32] Zhu R G, Yu H, Lu R H, Han S S, Huang Z F and Wan J 2020 Ghost imaging based on Y-net: a dynamic coding and conjugate-decoding approach *Opt. Express* **28** 17556–69
[33] Shang R B, Hawlik K H, Wang F, Situ G H and Luke G P 2021 Two-step training deep learning framework for computational imaging without physics priors *Opt. Express* **29** 15239–54
[34] Kumar S, Bu T, Zhang H, Huang I and Huang Y-P 2021 Single-pixel image classification via nonlinear optics and deep neural network *2021 Conf. on Lasers and Electro-Optics (CLEO)* 1–2
[35] Yu Y, Zheng J, Chen S and Yang Z 2022 Moving target imaging via computational ghost imaging combined with artificial bee colony optimization *IEEE Trans. Instrum. Meas.* **71** 1–7 Art no. 4502107
[36] Wang F, Wang H, Wang H C, Li G W and Situ G H 2019 Learning from simulation: an end-to-end deep-learning approach for computational ghost imaging *Opt. Express* **27** 25560–72
[37] Lyu M, Wang W, Wang H, Wang H C, Li G W, Chen N and Situ G H 2017 Deep-learning-based ghost imaging *Sci. Rep.* **7** 17865
[38] Li F Q, Zhao M, Tian Z M, Willomitzer F and Cossairt O 2020 Compressive ghost imaging through scattering media with deep learning *Opt. Express* **28** 17395–408
[39] Zhao J, Tang Z, Shao K and Pan S 2020 Computational spectral-domain ghost imaging based on hadamard modulation *International Topical Meeting on Microwave Photonics (MWP)*. 253–5 **2020**
[40] Li M F, Mo X F, Zhao L J, Huo J, Yang R, Li K and Zhang A N 2016 Single-pixel remote imaging based on Walsh-Hadamard transform *Acta Phys. Sin.* **65** 064201
[41] Luo B, Yin P Q, Yin L F, Wu G H and Guo H 2018 Orthonormalization method in ghost imaging *Opt. Express* **26** 23093–106
[42] Xu C, Li D, Guo K, Yin Z and Guo Z 2023 Computation ghost imaging with key-patterns for image encryption *Opt. Commun.* **537** 129190
[43] Li D, Lin B, Wang X and Guo Z 2022 High-performance polarization remote sensing with the modified U-net based deep-learning network *IEEE Trans. Geosci. Electron.* **60** 5621110
[44] Huang G, Liu Z, Maaten L V D and Weinberger K Q 2017 Densely connected convolutional networks *IEEE Conf. on Computer Vision and Pattern Recognition (CVPR, 2017)* 2261–9
[45] Li S, Deng M, Lee J, Sinha A and Barbastathis G 2018 Imaging through glass diffusers using densely connected convolutional networks *Optica.* **5** 803–13
[46] Breugnot, Sebastien, Clemenceau and Philippe 2000 Modeling and performances of a polarization active imager at =806 nm *Opt. Eng.* **39** 2681–8
[47] Christopher J C B, Yann L C and Corinna C MINST handwritten digit databasehttp://yann.lecun.com/exdb/mnist/ 1998

[48] Chen L C, Zhu Y K, Papandreou G, Schroff F and Adam H 2018 Encoder-decoder with atrous separable convolution for semantic image segmentation *European conference on computer vision (ECCV, 2018)*. 833–51
[49] Zhang X Y, Zhou X Y, Lin M X and Sun J 2018 Shufflenet: an extremely efficient convolutional neural network for mobile devices *IEEE/CVF Conf. on Computer Vision and Pattern Recognition (CVPR,2018)*. 6848–56